



# Development and application of a heated in-situ SEM micro-testing device



R. Fritz, D. Kiener\*

Department Materials Physics, Montanuniversität Leoben, Leoben, Austria

## ARTICLE INFO

### Article history:

Received 19 June 2017

Received in revised form 7 July 2017

Accepted 10 July 2017

Available online 12 July 2017

### Keywords:

In-situ testing

Elevated temperature

Micromechanics

Ultrafine-grained microstructure

Fracture toughness

## ABSTRACT

Understanding temperature-dependent deformation behaviour of small material volumes is a key issue in material science, especially the deformation behaviour of bcc metals at elevated temperatures is of particular interest for small-scale structural applications. Therefore, a custom-built heating device consisting of independently resistive-heated sample and indenter, and adaptable to existing micro-indenters, is presented. Key parameters of material selection, design of components and temperature control are outlined. Testing temperatures ranging from room temperature up to  $\sim 300$  °C are reached with low drift and without active cooling. To demonstrate the functionality, a variety of in-situ SEM micromechanical experiments were conducted at room temperature and 230 °C, respectively. Examples of micro-pillar compression on single crystalline and ultrafine-grained Chromium, as well as notched cantilever fracture experiments on ultrafine-grained Chromium show assets of this powerful tool, allowing more detailed insights into temperature-dependent deformation and fracture behaviour.

© 2017 The Authors. Published by Elsevier Ltd. This is an open access article under the CC BY license (<http://creativecommons.org/licenses/by/4.0/>).

## 1. Introduction

Measurement techniques to determine small-scale deformation behaviour at elevated temperature are increasing in popularity since several years. Initially, ex-situ nanoindentation techniques at elevated temperature [1–3] were used to determine mechanical properties such as Hardness or Young's Modulus of a large variety of materials [4–7], and further enhanced to investigate incipient plasticity [8–10]. By increasing test temperatures, the complexity of instrumental setups increased ensuing the purpose of minimizing thermal drift and oxidation problems [1,5,11]. To reduce such inaccuracies, several attempts are reported in literature. Exemplary, testing equipment is purged with inert gases [12–15] or relocated into a vacuum chamber [16–20] to minimize remaining impurities in the atmosphere or to reduce thermal drift and noise.

Parallel to the ongoing development of ex-situ nanoindentation experiments at elevated temperature, in-situ testing techniques inside a scanning electron microscope (SEM) performed at room temperature (RT) became popular [21,22]. By combining instrumented small-scale indentation techniques with the advantages of an SEM, such as high vacuum, vibration damping and direct observation of dynamic processes, a powerful tool to investigate material behaviour in-situ at non-ambient conditions became

available [17–19]. Wheeler et al. [23] were the first to report about an advanced in-situ SEM measurement approach up to 200 °C. Initially, the system was used to perform in-situ nanoindentation experiments on bulk metallic glasses utilizing a cube corner indenter to correlate measured load-displacement curves with surface shear offset displacements as a function of temperature. However, independent heating and temperature monitoring of sample and indenter was shown to be mandatory [11,24], as temperature gradients are responsible for drift issues. Heating of sample and indenter might be achieved by resistive [11,16,24] or laser heating equipment [25,26]. To reach temperatures above 300 °C, a cooling system to minimize thermal drift would be necessary [11,24].

Once the device operates stable at elevated temperature, attention has to be paid to temperature calibration and balancing issues. To calibrate contact temperatures, Wheeler et al. [27] discussed several potential ways to assess unavoidable thermal gradients within the limited hot zone. One approach is to indent the respective thermocouples used for temperature monitoring and to measure thermal drift by the use of a pre-set dwell time. Besides that, Raman spectroscopy was suggested as a non-contact technique and an accuracy of  $\pm 10$  °C was reported [27]. Additionally, a temperature matching procedure [24] placing sample and indenter into contact was developed to balance isothermal contact temperatures, instead of measuring displacement drift as conducted in earlier approaches [11].

Nowadays, in-situ platforms with temperature ranges spanning from  $-140$  °C [28–31] up to 800 °C [26] are available. Constraints

\* Corresponding author at: Jahnstraße 12, 8700 Leoben, Austria.

E-mail address: [daniel.kiener@unileoben.ac.at](mailto:daniel.kiener@unileoben.ac.at) (D. Kiener).

such as condensation of moisture for low temperature testing and oxidation issues at elevated temperature have to be taken into account. With that in mind, ex-situ or in-situ investigation of temperature-dependent material behaviour became widely accessible. Due to the limited availability of heatable in-situ SEM testing devices, most of the literature up to now deals with ex-situ nanoindentation [32,33] and pillar compression inside a vacuum chamber [34]. Only a few reports about in-situ investigations to study temperature dependent material behaviour were conducted on bcc [34], fcc [35] or hcp metals [36].

To further explore thermally activated deformation processes in bcc metals and to correlate instrumented testing data with occurring deformation mechanisms on small-scaled samples, this work describes the development, and first experiments on a custom-built in-situ heating device which can be re-fitted to an existing micro-indenter in an SEM. Special focus is put to material selection, efficient design of components and temperature control. Moreover, finite element simulations were conducted to get knowledge about unavoidable temperature gradients. The capabilities of the described system are exemplarily shown by performing in-situ micro compression tests on taper-free, single crystalline (sxx) and ultrafine-grained (ufg) Cr pillars, as well as notched cantilever fracture experiments on ufg Cr to evaluate fracture toughness values between RT and 300 °C. Moreover, obtained flow stress data were compared with results obtained from macroscopic tests and served to validate experiments.

## 2. Materials and methods

### 2.1. SEM and attached micro-indenter

The utilized indenter positioning system is attached to the chamber of an SEM (Zeiss LEO 982, Oberkochen, Germany, Fig. 1a) to save operational space. Several flanges for signal feed-throughs (indenter control, power supply, thermocouples) are provided on the wall of the vacuum chamber door. An Everhart Thornley Detector (SE-detector) as well as an In-Lens detector are installed for imaging purposes and an attached plasma cleaner (XEI Scientific Inc., Redwood City, USA) is available to remove organic residues. The sample is mounted on a separately controlled stage (Fig. 1b) and the UNAT-SEM micro-indenter (Zwick GmbH & Co. KG, Ulm, Germany) used for testing is shown in detail in Fig. 1c, already modified by the heating device. Initially, this micro-indenter was first described in [17]. In the present setup of the SEM, four axes ( $x_1, y_1, z_1, r_1$ ) allow to position the sample to coincide with the electron beam (Fig. 1b). In-plane alignment is achieved by  $x_1$  and  $y_1$ ,  $z_1$  is used to adapt the working distance and  $r_1$  allows to rotate the sample to align it with the indenter loading axis. Four axes on the indenter side ( $x_2, y_2, z_2, r_2$ ) allow to position the indenter into the electron beam (Fig. 1c).  $x_2$  and  $y_2$  are necessary for in-plane positioning,  $z_2$  and  $r_2$  for adapting the desired working distance and inclination angle. The ranges of indenter and sample movement are summarized in Table 1.

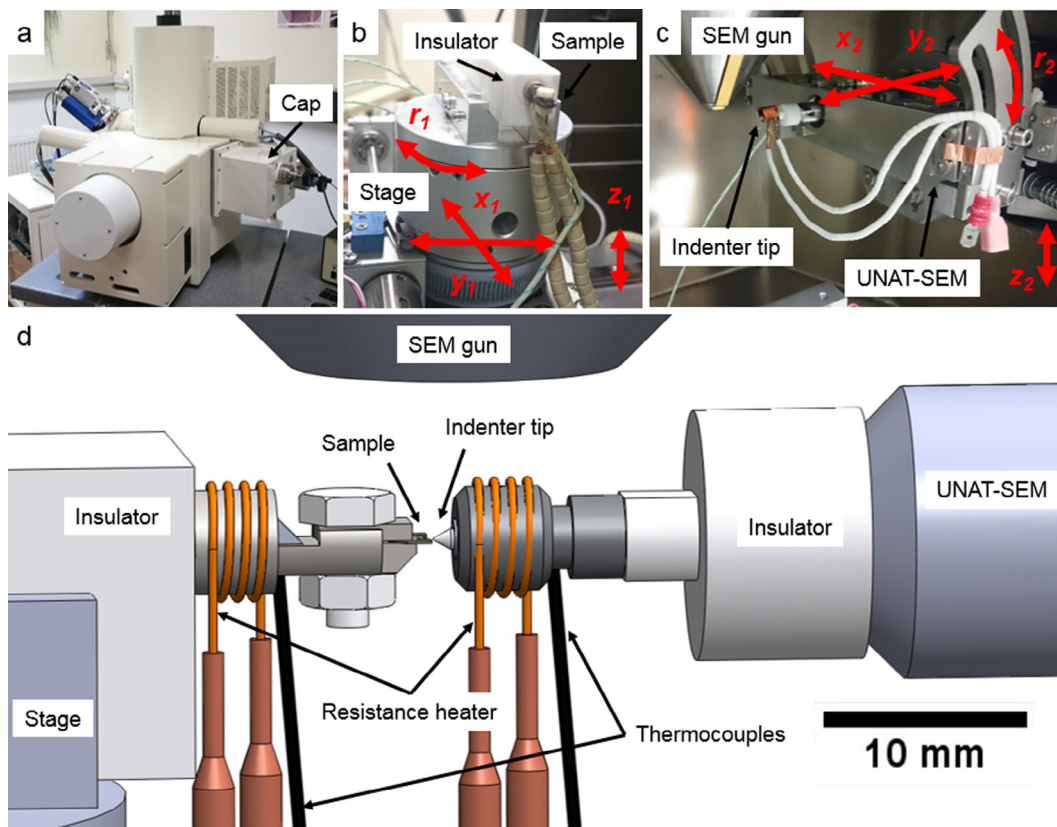


**Fig. 1.** Schematic of the present high temperature in-situ SEM testing setup. (a) Adapted SEM with cap (right) containing the micro-indenter and positioning stage. SEM stage (b) and micro-indenter (c), adapted with custom-built heating devices. Red arrows indicate available positioning axes. (d) Detail of heated parts inside the SEM chamber. (For interpretation of the references to colour in this figure legend, the reader is referred to the web version of this article.)

**Table 1**  
Motion ranges of the sample stage and indenter, as well as the specifications of the SEM and micro-indenter in the present setup.

SEM		Micro-indenter	
$x_1$	$\pm 75$ mm	$x_2$	$\sim 50$ mm
$y_1$	$\pm 75$ mm	$y_2$	$\sim 50$ mm
$z_1$	$\pm 25$ mm	$z_2$	25 mm
$r_1$	$360^\circ$	$r_2$	$0-25^\circ$
Filament type	Field emission gun	Max. displacement	$\pm 50$ $\mu$ m
Acceleration voltage	1–30 kV	Noise level of displacement measurement	<1 nm
Typical system vacuum	$6 \cdot 10^{-5}$ mbar	Max. force	$\pm 500$ mN
Typical column vacuum	$1 \cdot 10^{-9}$ mbar	Noise level of force measurement	<10 $\mu$ N
		Travel range of the piezo actuator	>100 $\mu$ m
		Maximum voltage of the piezo actuator	–20 V to +120 V

## 2.2. Material selection

To develop an in-situ heating device, material selection for all components is of major importance. As the heating device operates in vacuum atmosphere, materials with considerably high vapour pressure and a sufficient service temperature are crucial. Service temperature in this context describes the maximum temperature where a material can be used for an extended time period without significant deformation, oxidation, chemical reactions, loss of strength or creep, or other primary properties for which the material is normally used [37]. Only non-magnetic materials are advised inside an SEM, and diffusional processes and chemical reactions must be taken into account when sample and indenter get in contact at elevated temperature [3]. Moreover, the coefficient of thermal expansion (CTE) should be in the same range for materials which are in direct contact. There is high demand for minimized

material volumes to enable localized heating to permit fast heating rates, as well as requirements regarding operational space inside the SEM (working distance  $\sim 5$  mm). Fig. 1d shows a detail of heated parts within the SEM chamber. The material selection process of each component is described below and material properties are listed in Table 2.

Wheeler et al. [3] summarized several benefits and disadvantages of indenter materials. To choose an appropriate one, Ref. [3] was used as a guideline for the selection process. Parameters such as oxidation resistance, high melting point as well as high Young's Modulus and hardness are obligatory. High specific heat capacity ( $c_p$ ), electrical resistivity ( $R$ ) as well as machinability are necessary, and therefore only a small number of eligible materials such as diamond, some carbides ( $B_4C$ , SiC, WC), nitrides (cBN), oxides ( $Al_2O_3$ ) and metal composites such as WC-Co remain suitable. Moreover, the increased diffusivity of dopants at elevated temperature has to be taken into account. A classic example regarding diffusional problems is the indentation of low carbon steel with metastable diamond [3] or indentation of pure tungsten with a WC indenter tip. As soon as indenter and sample are in contact, in both cases carbon might diffuse at elevated temperature from the carbon rich indenter side to the indented metal as long as concentration gradients remain present. In the present case, Sapphire ( $Al_2O_3$ ) was utilized as material for the flat punch indenter tip, shown in Fig. 2a. Initially, a conductive Sapphire Berkovich indenter tip was obtained from Synton MDP AG (Nidau, Switzerland) to perform nanoindentation experiments. At a later time, the tip of the indenter was prepared to a flat punch by FIB milling (Zeiss LEO 1540 XP, Oberkochen, Germany) to its final dimensions of  $\sim 10 \times 6 \mu m^2$ , as shown in Fig. 2a.

To conduct micro cantilever fracture experiments, a WC wedge was mechanically ground and subsequently FIB-milled to its final shape. WC was chosen as one of the most stable indenter materials, although it can be vulnerable in combination with tungsten or iron at elevated temperature [3]. As shown in Fig. 2b and c, the tip radius is  $\sim 500$  nm and the length of the wedge is  $\sim 120 \mu m$ .

**Table 2**  
Selected materials and decisive properties for the material selection process [37].

Material	Usage	$c_p$ [J/kg · K]	$\lambda$ [W/m · K]	$R$ [ $\Omega \cdot cm \cdot 10^6$ ]	CTE [ $10^6/K$ ]	$T_{service}$ [ $^\circ C$ ]
Mo	Tip holder	255–275	129–147	5.2–6	4.8–5.5	1310
V	Sample holder	480–505	28–32	19–30	8–8.6	530
Cu	Power supply lines, clamps	383–387	390–398	1.91–1.95	16.8–16.9	360
Constantan <sup>®</sup>	Resistive wire	410	23	0.49	13.5	600
Macor <sup>®</sup>	Screw joints, insulation	774–805	1.4–1.56	$10^{22}$ – $10^{24}$	12.7–13.2	730
Ceramabond <sup>®</sup> 569	Adhesive	–	20.5	–	7.6	1377
$Al_2O_3$	Flat punch	790–800	20–25.6	$10^{19}$ – $10^{21}$	8.8–9.2	1230
WC	Wedge	184–190	28–88	63.1–100	4.5–7.1	727

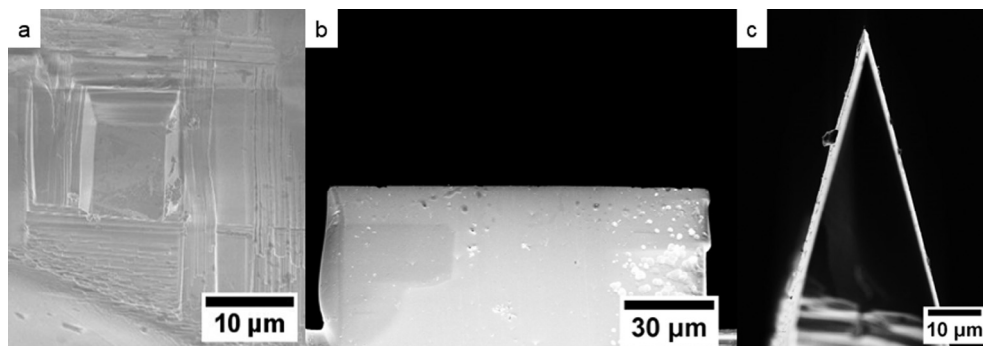


**Fig. 2.** Indenter tips suited for the heating device. (a) A  $10 \cdot 6 \mu m^2$  sapphire flat punch and (b and c) a WC wedge having a length of  $\sim 120 \mu m$ , a tip radius of  $\sim 500$  nm and an opening angle of  $\sim 30^\circ$ .

The CTE of Sapphire and WC restrict the material selection of the indenter tip holder (Fig. 1d), as they should equally expand during heating to minimize thermally induced stresses. Moreover,  $c_p$  as well as thermal conductivity ( $\lambda$ ) were maximized to bring and store thermal energy into the material. Only a few machinable metals such as Ta, Mo, Nb, Zr, Cr and V remain suitable within these restrictions. Mo and V were chosen to be the material of choice for the indenter tip holder and the sample holder, respectively (see Table 2 and Fig. 1d). As brazing and clamping of the miniaturized indenter tips is not straight forward to achieve, tips were instead glued to their holders using a high temperature adhesive (Ceramabond 569<sup>®</sup>), which is a two component ceramic bond providing a service temperature of 1650 °C. By increasing the amount of thinner, the viscosity of the glue was easily adjusted. A low viscosity in the present case was important, as the glue was sucked by capillary forces into the fitting of the indenter tip and the tip holder. Subsequently, the glue was cured in a convection oven for two hours at 94 °C.

To mount the lamella-shaped, macroscopic samples [38,39] on the heatable sample holder (Fig. 1d), they are fixed on the V holder by a screw made out of Macor<sup>®</sup> ceramic. This ceramic is machinable, resists high temperatures and provides a low  $\lambda$  and high  $R$ . Common screws in the size of a few millimetres are usually made from brass or low alloyed, magnetic steels and are therefore not well suited.

For exact temperature measurements, Type K (Chromel/Alumel) thermocouples with a temperature range of –200 °C to 1200 °C were utilized and brazed close to sample and indenter tip (Fig. 1d). An eutectoid 72Ag28Cu braze (Brazetec 7200, Ögussa GmbH, Vienna, Austria) providing a service temperature of 1300 K was used to fix the thermocouple at the indenter tip holder made out of Mo. Due to poor adhesion between the V sample holder and the eutectoid braze, an interlayer braze (Cu7Mn3Co, Brazetec 21-68, Ögussa GmbH, Vienna, Austria) was first brazed on the surface of the sample holder. The thermocouple was subsequently fixed using the eutectoid braze to the sample holder. More importantly, the thermocouples were attached to the holders before the indenter was glued into its shaft, as the braze melts at about 1000 °C. Zinc-based brazes as well as brass holders were neglected in the material selection process, as zinc might evaporate at a relatively low vapour pressure and alter the heating device as well as the SEM interior.

To reach a considerable high testing temperature, the resistive-heated filaments of choice must produce thermal energy efficiently. In the present case, filament wires had to be very flexible, as they need to be looped around the holders and stay in contact with them (Fig. 1d). In fact, filaments were formed to coils to ease their placement over the holders. They are made out of Konstantan<sup>®</sup>, a frequently used heating wire material having a wire diameter of 0.4 mm. It consists of 55% Cu, 44% Ni and 1% Mn. The Konstantan<sup>®</sup> coils are connected by Cu clamps to thicker Cu wires that directly lead to the chamber feedthroughs. The Cu wires are insulated with ceramic beads (Tectra GmbH, Frankfurt, Germany). To further thermally insulate the tip shaft of the micro indenter from heat, a ceramic spacer made out of Macor<sup>®</sup> is placed between the heated indenter tip and the indenter mechanics (Fig. 1c and d). Further, the heated sample holder is mounted on a Macor<sup>®</sup> spacer, which is fixed to the SEM stage to prevent heating, as shown in Fig. 1b and d.

### 2.3. Power- and temperature control

To resistively heat sample and indenter separately inside the SEM, a TOE 8952-20 dual-output DC power supply (Toellner Electronic Instruments GmbH, Herdecke, Germany) providing a voltage range of 0–20 V and a current range of 0–20 A was used. To properly measure the desired temperatures, thermocouples were connected to an USB TC-08 data logger (Pico Technology, St. Neots, UK) providing an accessible temperature range of –270 °C to 1280 °C. By converting voltage into temperature, sampling rates of up to 10 measurements per second are achieved. An automatic cold junction compensation is used to record corresponding temperatures at eight individual positions within the whole setup. Software control and temperature monitoring was implemented in LabView<sup>®</sup> (National Instruments Corp., Austin, Texas, USA), and temperature control was achieved using a PID feedback loop. An exemplary heating procedure up to ~230 °C, with sample and indenter being out of contact, is shown in Fig. 3a.

Within 30 min, a constant and stable temperature at both thermocouples is achieved, while the accuracy of the controlled temperatures is  $\pm 0.1$  °C, as shown in Fig. 3b and c. The situation of heated sample and indenter in contact requires temperature calibration and matching for various reasons [27]. Unfortunately, it is not possible to directly braze thermocouples on the micron-

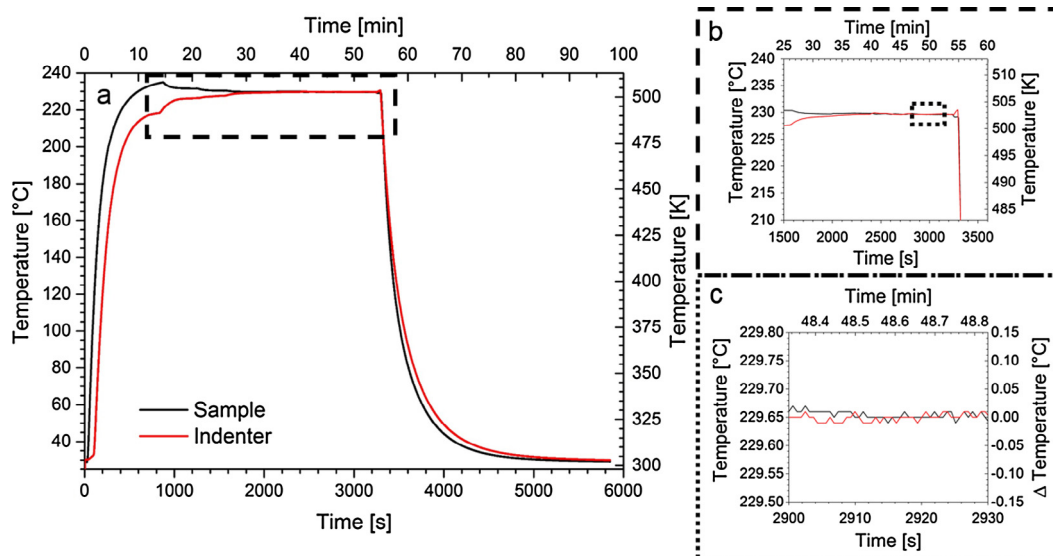


**Fig. 3.** Representative heating procedure of sample and indenter. (a) Stable heating to the desired temperature and subsequent cooling to RT is possible within 90 min. (b) After ~30 min, a constant temperature is achieved. (c) Temperatures can be adjusted with an accuracy of  $\sim 0.1$  °C.

sized samples or the indenter. Holders, samples and indenters are made out of different materials, and therefore exact temperature measurements are not possible. Wheeler et al. [3,24,27] suggested individual temperature calibration techniques as well as a temperature matching procedure, which is recommended before testing at elevated temperature. For further, more detailed information about temperature calibration, different to previous assessments we also utilized simulation approaches, as described in Section 2.4.

#### 2.4. Temperature calibration by numerical simulation

The full experimental setup was recreated true to original data in 3D using a CAD program. The geometry was loaded into the finite element program Abaqus (Dassault Systems, Providence, RI, USA) to conduct heat flow calculations. A biased mesh size was used with a coarser mesh for larger, less significant parts, while for micron-sized parts a very fine mesh has been utilized. Material properties used in the calculations are shown in Table 2. Moreover, convection within the vacuum chamber was neglected and characteristic radiation properties of each material as suggested in [37] were chosen. Sample and indenter were first placed out of contact and separately heated, as shown in Fig. 4. A constant, direct current and independent powers ( $P$ ) at the sample and indenter side were used to reach constant temperatures (268 °C) at the marked positions of the thermocouples after a heating time of 3600 s. Positions of thermocouples at the sample and the indenter holder are indicated in Fig. 4 as  $T_1^S$  and  $T_1^I$ , respectively. Resulting temperature gradients are presented as colour code in Fig. 4, indicating different absolute temperatures at the sample and the indenter tip. Those differences are of major importance and should be minimized when bringing sample and indenter in contact to perform elevated temperature experiments at minimum drift.

This situation is shown in Fig. 5a, where a flat punch indenter is in contact with a 1  $\mu\text{m}$  sized pillar. The details of the contact situation are shown in Fig. 5b and c. A large temperature gradient occurs although temperatures of thermocouples  $T_1^S$  and  $T_1^I$  are equilibrated. This results in thermal as well as displacement drift. To get rid of such inaccuracies, a detailed knowledge of remaining temperature gradients and the absolute temperature at the sample and the indenter are necessary.

To underline the importance of temperature calibration, the material of the tested lamella-shaped specimens was varied and temperature gradients were analysed, as shown in Fig. 6.  $T_2^S$  and  $T_3^S$  in Fig. 6a and b indicate individual positions of temperature measurement on the specimen fixation and directly at the pillar. Design limitations such as the distances between heated parts,

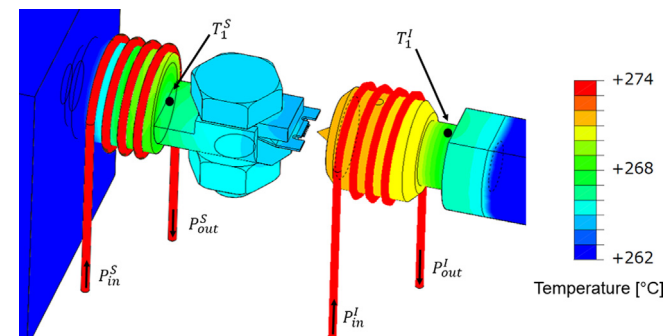


**Fig. 4.** Temperature distribution in heated parts inside the SEM. Temperature at individual thermocouples at sample ( $T_1^S$ ) and indenter ( $T_1^I$ ) is constant, but large temperature gradients and differences in absolute temperature at the sample and the indenter tip are observed. (For interpretation of the references to colour in this figure legend, the reader is referred to the web version of this article.)

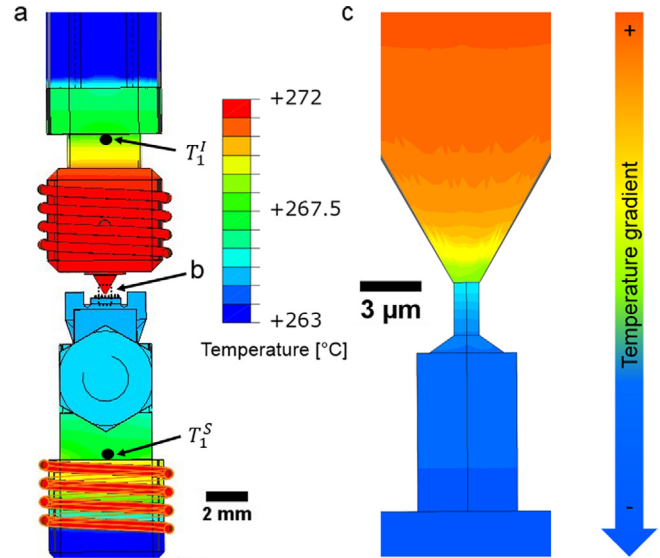


**Fig. 5.** Although the thermocouples  $T_1^S$  and  $T_1^I$  are at the same temperature (a), a large temperature gradient resulting in thermal drift occurs when bringing sample and indenter in contact (b). (c) Detail of the contact situation with a large temperature gradient. (For interpretation of the references to colour in this figure legend, the reader is referred to the web version of this article.)

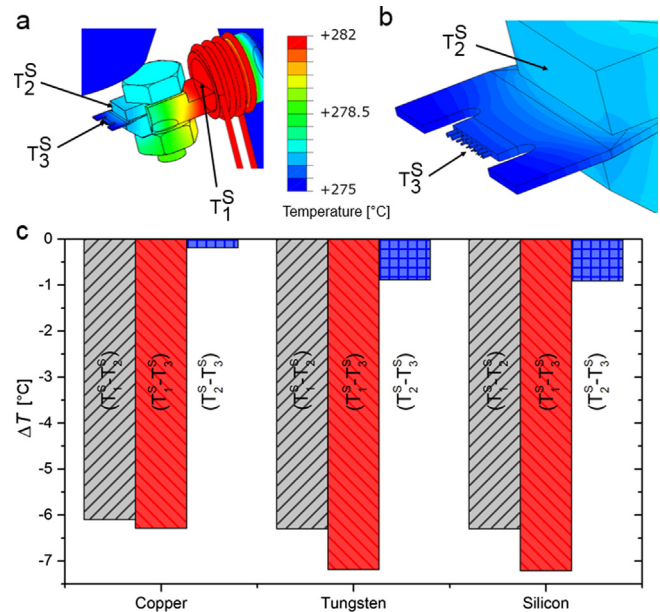


**Fig. 6.** Influence of varying specimen material on temperature gradients. (a) and (b) indicate local temperature distribution and positions of temperature measurement, the gradient of which are reported in (c). (For interpretation of the references to colour in this figure legend, the reader is referred to the web version of this article.)

thermocouples and the sample, as well as sample geometry are of major influence of temperature gradients, as shown in Fig. 6b. By heating different specimens with varying  $\lambda$  such as Cu, W or Si, it becomes evident that samples with high thermal conductivity such as Cu allow lower temperature gradients compared to W or Si samples (Fig. 6c). Nonetheless, within the present setup gradients up to 7 °C and more are possible between thermocouple and specimen, as thermal properties strongly influence the temperature distribution. Thus, to ensure equilibrium temperatures, a procedure to match sample and indenter tip temperature is inevitable before each experiment.

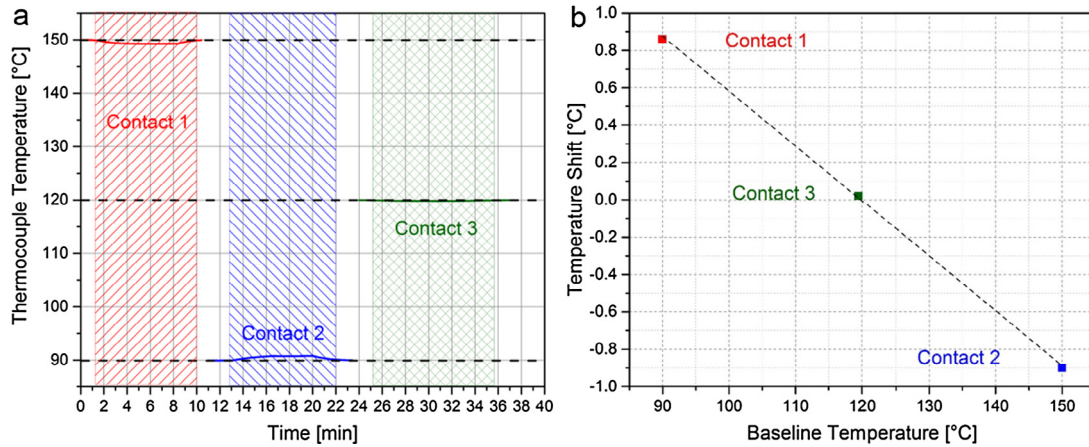


**Fig. 7.** (a) Exemplary temperature matching procedure to infer the isothermal contact temperature and (b) determining the zero-shift working temperature by linear extrapolation. The procedure was taken from [24]. (For interpretation of the references to colour in this figure legend, the reader is referred to the web version of this article.)

### 2.5. Temperature matching

Fig. 7a presents a temperature matching procedure as suggested in [24] conducted with the present setup. Thereby, sample and indenter are brought into contact several times and temperature shifts are analysed in a hold period at pre-defined, constant low load to minimize creep influences. In the first contact situation, as shown in Fig. 7a, the cold tip and the hot sample, for example, are not in equilibrium causing a temperature drop on a thermocouple as well as displacement drift. Contact situation two shows the same non-equilibrium condition for the opposite temperature misadjustment, exemplary shown for a cold sample and a hot indenter situation. To balance the contact temperature, this procedure has to be repeated until temperature change is minimized during contact, indicating zero temperature shift (Contact 3), where no detectable temperature difference between tip and sample is observed. This process can be linearly extrapolated to zero shift and is shown in Fig. 7b. Subsequently, the setup is ready to perform experiments at the adjusted elevated temperature.

### 2.6. Material preparation

An sxx Cr rod oriented in (1 0 0) was obtained from Mateck GmbH (Jülich, Germany) and the polycrystalline Cr was provided as sheet by Plansee SE (Reutte, Austria). The polycrystalline Cr was deformed via HPT [40,41] to reach an ufg microstructure. A pressure of 4.2 GPa at 200 °C and a rotational speed of 0.5 rpm for 50 rotations resulted in an equivalent strain of ~360 and a grain size of ~160 nm [42]. No pronounced texture, but slightly elongated grains with an aspect ratio of ~3:1 were observed in the as-deformed microstructure in axial direction. Wire cutting, sample polishing and ion milling [38,39] as well as FIB preparation of the non-tapered pillars using milling currents of 1 nA and 100 pA for rough cutting and final polishing, respectively, were used. Pillar fabrication with a size range of ~0.2 μm – 6 μm and an aspect ratio of 3:1 was initially described in [39,42]. Moreover, 9 · 9 · 45 μm<sup>3</sup> sized cantilevers were milled from an ufg Cr lamella. Due to larger sample sizes, milling currents of 5 nA for rough cutting and 500 pA for final polishing were used. To initiate a pre-crack in the cantilevers, FIB notches were fabricated using the line-milling mode. A FIB current of 500 pA and a milling time per length of milling of 6.5 s/μm resulted in a notch depth of ~1.5 μm. Both sample geometries were fabricated in axial direction with respect to the HPT orientation and load was applied perpendicular to elongated grains. A similar preparation process was initially shown and further detailed in [43]. Tests were carried out utilizing the above

described SEM with the attached micro-indenter as described in Section 2.1. To analyse crack growth of the pre-notched cantilevers and the dynamics of the compressive deformation, images during in-situ testing were captured with 1 frame per second. High resolution SEM images (Zeiss LEO 1525, Oberkochen, Germany) were recorded after deformation to analyse the resultant surface evolution. Finally, cross sections were milled into the highly deformed zones of the cantilevers to investigate the microstructure as well as crack propagation during elevated temperature testing.

### 2.7. Data analysis

All tests were conducted in displacement-controlled mode. For compression tests, a constant nominal strain rate of  $3 \cdot 10^{-3} \text{ s}^{-1}$  was applied and pillars were deformed to ~20% strain. Recorded force-displacement data was corrected to take into account the stiffness of the lamella [44], and sample sink-in [45] was considered. Additional weight acting on the force transducer (~10 g) of the indenter tip shaft, including the thermocouple and the resistive wire, affect the force measurement by a lateral load. Therefore, the transducers were calibrated before conducting the experiments by performing air indentations over the whole displacement range of the transducer. The resultant positive slope of the force-displacement signal was then used to correct the signals to zero-load.

Engineering stress was calculated by taking the top pillar area into account and engineering strain was calculated using the height of the non-tapered pillars.

Cantilevers were bent utilizing a displacement rate of 1 μm/min, as suggested in [43] and deformed to a maximum load line displacement of 8 μm, which corresponds to a bending angle of ~15°. To investigate fracture morphologies and to open the crack tip, cantilevers were further bent downwards. Width ( $W$ ), height ( $B$ ), bending length ( $L$ ) and crack length ( $a_0$ ) of the specimens are shown in Table 3. They were used to calculate fracture toughness values according to [46]

$$K_Q = \frac{F_Q \cdot L}{B \cdot W^{3/2}} \cdot f\left(\frac{a}{W}\right). \quad (1)$$

The force  $F_Q$  was determined according to ASTM E-399 [46], and the geometry factor  $f(a/W)$ , which describes the influence of the pre-crack, was taken from [47]. As requirements for plane strain fracture toughness are not fulfilled, results are presented as conditional fracture toughness values and indicated with the subscript “Q”.  $K_Q$  determined this way gives a lower limit for fracture toughness [43]. As linear elastic fracture mechanics (LEFM) is only applicable for hard and brittle materials, the  $J$ -integral approach is

**Table 3**  
Cantilever dimensions and conditional fracture toughness values at RT and 230 °C for ufg Cr in axial direction.

Temperature	$W$ [ $\mu\text{m}$ ]	$B$ [ $\mu\text{m}$ ]	$L$ [ $\mu\text{m}$ ]	$a_0$ [ $\mu\text{m}$ ]	$K_Q$ [ $\text{MPa m}^{1/2}$ ]	$K_{QJ}$ [ $\text{MPa m}^{1/2}$ ]
RT	8.834	8.989	37.3	1.589	2.43	16.98
230 °C	7.995	9.340	32.5	1.805	1.43	16.81

commonly used for large-scale yielding of small samples. According to ASTM E 813–89 [48],  $J$  is given as the sum of elastic and plastic components

$$J = \frac{K_Q^2 \cdot (1 - \nu^2)}{E} + \frac{\eta \cdot A_{pl}}{B \cdot (W - a_0)}, \quad (2)$$

where  $\nu = 0.21$  is the Poisson ratio,  $E = 294$  GPa is the Young's Modulus of Cr [49],  $\eta = 2$  is a constant and  $A_{pl}$  represents the plastic work of the experiment (area beneath the load-displacement curve).  $J$ - $\Delta a$  curves were calculated and fitted according to [43] using crack extension values obtained from the in-situ experiment at each step of unloading. To compare fracture toughness values from elastic plastic fracture mechanics (EPFM,  $J$ -integral) with LEFM ( $K_Q$ ),  $J$  is converted to

$$K_{QJ} = \sqrt{\frac{J \cdot E}{1 - \nu^2}}, \quad (3)$$

which gives an upper bound for fracture toughness values [43].

### 3. Results

Fig. 8a shows representative engineering stress-strain curves of pillar compression experiments at RT (black) and 230 °C (red) on ufg Cr (solid line) and sxx Cr (dashed line). Yield stress values at RT of  $\sim 400$  MPa and  $\sim 100$  MPa at 230 °C were measured for sxx Cr. Refining the microstructure into the ufg regime leads to an increase of yield strength to  $\sim 1100$  MPa and 950 MPa at RT and 230 °C, respectively, according to Hall and Petch [50,51]. Fig. 8b and d shows deformed ufg pillars, and Fig. 8c and e presents deformed sxx samples, at RT and 230 °C, respectively. To further provide detailed knowledge of ongoing deformation mechanisms in ufg Cr, cantilever fracture experiments were designed using the obtained uniaxial test data.

Results of cantilever fracture experiments in terms of bending stress-displacement plots and post-deformation SEM images of ufg fracture samples, deformed at RT (black) and 230 °C (red) are shown in Fig. 9. To compare yield stress values with results obtained by uniaxial testing (Fig. 8), stresses were calculated using the remaining ligament size  $W - a_0$ . Fig. 9a depicts typical linear elastic loading of the cantilevers followed by a transition into the plastic regime. Strain hardening up to a displacement of  $\sim 4$   $\mu\text{m}$  is observed by a subsequent softening until the maximum displacement of 8  $\mu\text{m}$  was reached. Fig. 9b–d and e–g show deformed cantilevers and corresponding fracture morphologies at the respective temperatures. The crack propagation is clearly affected by the testing temperature (Fig. 9c and f), indicated by red arrows. At RT, the extending crack deflects and propagates perpendicular to the loading direction, while at 230 °C blunting without crack extension nor crack deflection is observed. This behaviour is also reflected by the varying fracture morphology presented in Fig. 9d and g, where an inclined view into the opened cracks is shown.

### 4. Discussion

#### 4.1. Numerical simulation

The conducted numerical simulation indicates material- as well as sample geometry-dependent temperature gradients if

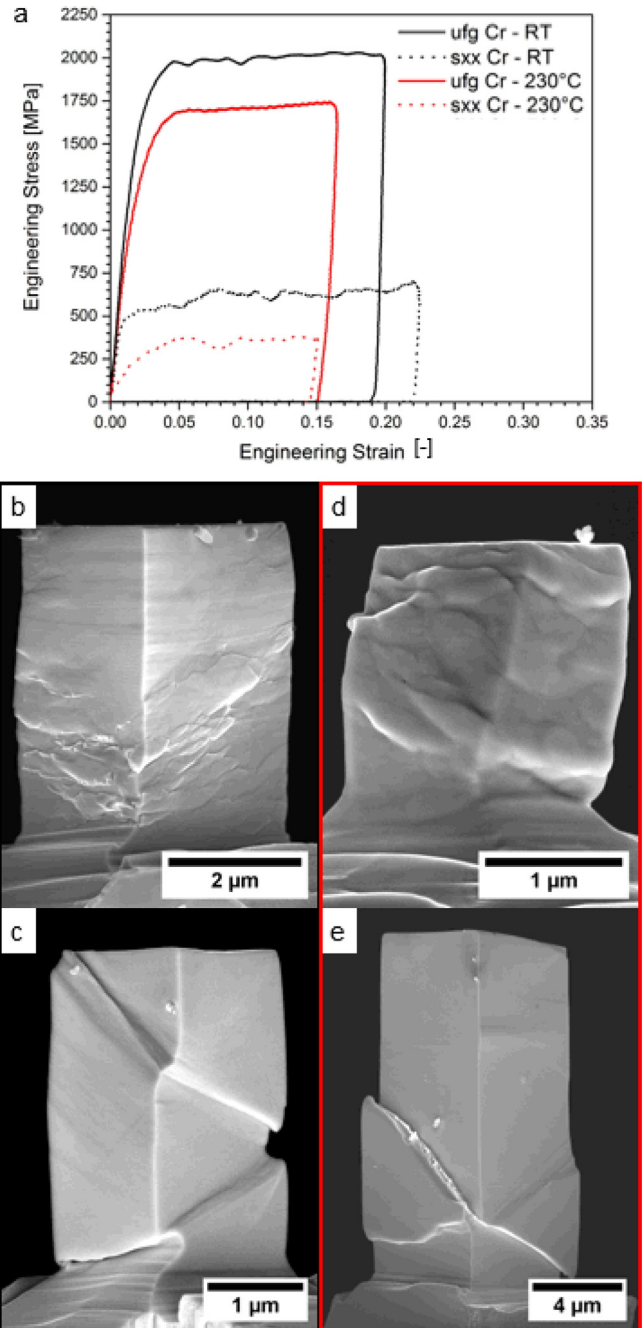


**Fig. 8.** (a) Engineering stress-strain curves showing the deformation behaviour of ufg (solid lines) and sxx (dashed lines) Cr pillars at RT (black) and 230 °C (red). (b–e) Post compression SEM images of deformed pillars. (b) and (c) show deformed ufg and sxx pillars at RT, (d) and (e) present an ufg and an sxx pillar, respectively, deformed at 230 °C. (For interpretation of the references to colour in this figure legend, the reader is referred to the web version of this article.)

temperatures at the indicated thermocouples are equilibrated. The knowledge of such gradients is of major importance regarding measurements at non-ambient conditions and helps minimizing thermal drift. Moreover, numerical simulations are inevitable if a

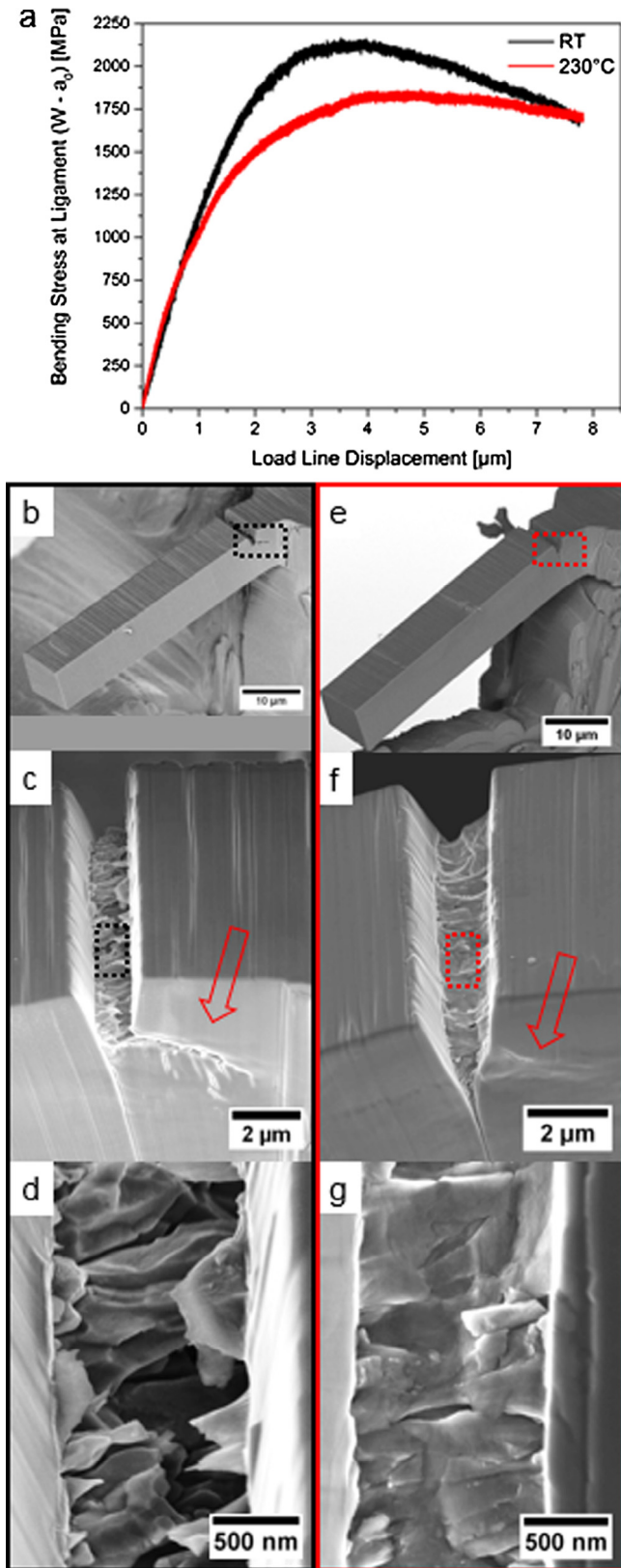


**Fig. 9.** (a) Bending stress–displacement curves of notched ufg cantilevers deformed at RT (black) and 230 °C (red). (b–g) depict details of the fracture morphologies at corresponding temperatures. (For interpretation of the references to colour in this figure legend, the reader is referred to the web version of this article.)

temperature matching procedure is not feasible due to limitations of the sample geometry e.g. by testing samples on needle-shaped specimens at elevated temperatures [44,52].

#### 4.2. Pillar compression

Literature values of macroscopic yield stresses for sxx Cr at RT [53] are found to be  $\sim 300$  MPa in (100) orientation for tensile experiments, and failure occurred by void nucleation and coalescence. In the present case, a sample size effect leading to yield stresses of  $\sim 400$  MPa is expected within the size regime of a few microns, as shown by Uchic et al. [54]. Size effects in sxx Cr are separately discussed in [42].

The flow stress decrease in ufg Cr at 230 °C (Fig. 8a) partly results from a grain size increase, as well as a vanishing contribution of the thermal stress component, as commonly observed in bcc metals at elevated temperature [33]. Fig. 10a and b present the undeformed microstructures in the ufg Cr lamella at RT and 230 °C. The mean grain size increased from  $\sim 160$  nm to  $\sim 350$  nm and a reduction of grain aspect ratio was observed. An estimation of the flow stress decrease by simple Hall-Petch relation [50,51] results in a flow stress reduction of 200 MPa. The Hall-Petch coefficient of Cr ( $k_{H-P} = 1380 \text{ MPa}\mu\text{m}^{1/2}$ ) was taken from [55]. Moreover, flow stress values of sxx (530 MPa) as well as ufg Cr (2050 MPa) obtained by nanoindentation [33] and macroscopic tests [42] at RT and elevated temperature are well within the range of flow stress values obtained with the present heating setup.

Post compression SEM images of ufg pillars as shown in Fig. 8b and d show no distinct differences. SEM images of sxx pillars (Fig. 8c and e) indicate differences in deformation behaviour. The propagation of screw dislocations via cross-slip is the rate-limiting mechanism at low temperatures in bcc metals [56]. Considering the sample surface in Fig. 8c, slip steps are not well-defined, which gives evidence of cross-slip processes. At elevated temperature the surface morphology in Fig. 8e reveals sharp slip steps, indicating reduced cross-slip of screw dislocations due to thermal activation [34]. Moreover, the decrease in flow stress from  $\sim 400$  MPa at RT to  $\sim 100$  MPa at 230 °C in sxx samples indicates a decrease of the thermal stress component of  $\sim 300$  MPa.

#### 4.3. Fracture processes

Fracture toughness of semi-brittle materials such as bcc metals is mostly investigated on sxx samples [43,57–62]. For polycrystalline samples with defined pre-notches, only few ex-situ [63–68] and in-situ studies [69] are found in literature. Fracture toughness and deformation behaviour of bcc metals are strongly dependent on strain rate, grain size and temperature [33,70]. Thermal activation reduces the high Peierls stress and therefore eases the movement of screw dislocations. This results in a semi-brittle deformation behaviour for a specific microstructure and loading condition, indicated by a specific ductile-to-brittle transition temperature (DBTT) [71].

Bohnert et al. [61] showed that fracture toughness values of sxx W are strongly dependent on notch geometry, which was also supported by finite element simulations. In contrast to that, fracture toughness values are not significantly influenced by the miniaturized specimen geometry, as long as assumptions for large-scale yielding are made. The effect of notch type on fracture toughness was investigated by Wurster et al. [43], where fracture toughness values of natural notched sxx W cantilevers were compared to FIB-notched cantilevers. No influence of notch type as well as

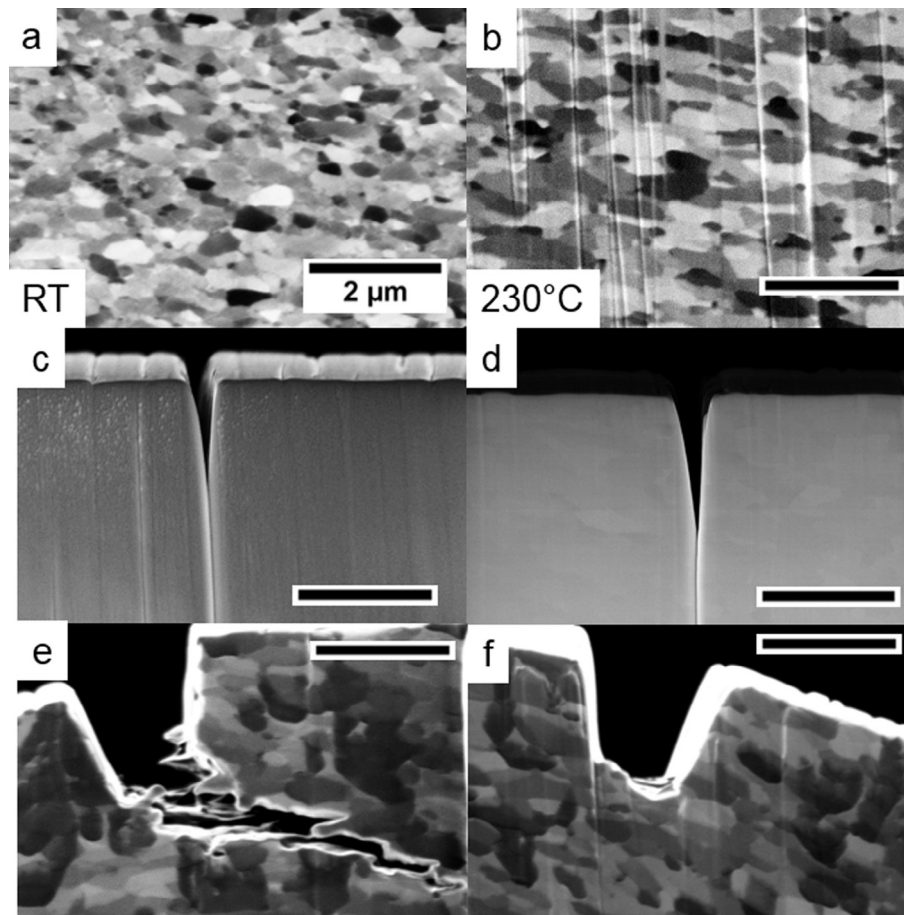


**Fig. 10.** Comparison of microstructure as well as cross sections of the deformed cantilevers. Undeformed ufg Cr microstructure at RT (a) and 230 °C (b). The mean grain size increased from ~160 nm to ~350 nm. (c) and (d) show details of the pre-notches. (e) Crack deflection along the orientation of elongated grains at RT. (f) At 230 °C plastic deformation and crack tip blunting without crack growth is observed.

specimen size were reported in the micron regime. Fracture toughness of polycrystalline, macroscopic samples was summarized in [64], indicating that fracture mechanisms for ufg metals differ from large-grained samples. Cantilevers in the present case are well below sample dimensions investigated in [64]. Approx. 2500 grains are located within the cantilever cross section. The lower limit of fracture toughness's ( $K_{Q0}$ ) as well as upper limits ( $K_{QJ}$  from  $J$ -Integral) are summarized in Table 3. Fig. 10c and d show details of the pre-notched samples. No distinct differences are observed before testing, which might be reflected by comparable fracture toughness values at RT and 230 °C. All values are expected to lie below the characteristic DBTT of Cr, which is between 320 °C and 390 °C in the undeformed condition [72]. Moreover, yield stresses of uniaxial deformed samples (1100 MPa at RT and 950 MPa at 230 °C) and cantilever fracture experiments (1130 MPa at RT and 910 MPa at 230 °C) indicate comparably plastic limits for the different testing techniques. However, post deformation SEM images (Fig. 9) do reveal differences related to crack initiation and propagation. At RT, the cantilever fails at the pre-notch and the crack immediately deflects and extends perpendicular to the loading direction (Fig. 9b and c). Moreover, grains were pulled out of the fracture surface (Fig. 9d). Blunting instead of crack extension and crack deflection was observed in SEM images of the cantilever deformed at 230 °C (Fig. 9e–g). Grains tended to show a more ductile behaviour compared to RT. Fig. 10e and f shows FIB cross sections of the highly deformed zone of the cantilevers at RT and 230 °C, respectively, and confirm different deformation behaviour. At RT, the crack propagated on an intercrystalline crack path in the

direction of the elongated grain structure. Such phenomena was already shown in [63,64]. No transgranular fracture was expected, as the grain size was too small for sufficient pile-up within the grains [64]. Decohesion processes at the grain boundaries were observed on triple junctions. At 230 °C, blunting instead of crack extension was observed (Fig. 10f). However, both experiments show that grain boundaries act as an effective barrier against crack growth [69]. While the crack extension in ufg Cr along grain boundaries is indicative for the RT experiment, blunting around the pre-crack was observed at elevated temperature.

## 5. Conclusion

The development and characterization as well as first experiments on a custom-built in-situ heating device were presented. A maximum temperature of 300 °C was shown to be achievable by separately resistive-heated indenter and sample. Finite element simulation results underline the importance of appropriate temperature calibration procedures followed by exact temperature matching. Quantitative in-situ experiments such as pillar compression and cantilever fracture testing at elevated temperatures were shown to be possible with high resolution inside the SEM. Pillar compression experiments on single crystalline as well as ultrafine-grained Chromium samples reveal an expected flow stress decrease due to a reduced thermal stress component, which goes along with a temperature-induced change of the microstructure in ultrafine-grained Chromium. Cantilever-based fracture experiments on ultrafine-grained Chromium show almost constant

fracture toughness values at RT and 230 °C, although crack propagation and crack deflection mechanisms already changed with increasing temperature towards more ductile deformation.

## Acknowledgements

The authors want to thank Manuel Petersmann from the Institute of Mechanics at the Montanuniversity at Leoben for help with Abaqus simulation, Dr. Thomas Schöberl from ESI for selecting and brazing the specific brazes on the holders, and Dr. Wolfram Knabl from Plansee SE for providing the high purity Chromium material. Financial support by the Austrian Federal Government represented by the Austrian Science Fund FWF (project number: P25325-N20) is gratefully acknowledged.

## References

- [1] C.A. Schuh, C.E. Packard, A.C. Lund, Nanoindentation and contact-mode imaging at high temperatures, *J. Mater. Res.* 21 (2006) 725–736, <http://dx.doi.org/10.1557/jmr.2006.0080>.
- [2] Z.C. Duan, A.M. Hodge, High-temperature nanoindentation- new developments and ongoing challenges, *JOM.* 61 (2009) 32–36, <http://dx.doi.org/10.1007/s11837-009-0177-5>.
- [3] J.M. Wheeler, J. Michler, Invited article: indenter materials for high temperature nanoindentation, *Rev. Sci. Instrum.* 84 (2013) 101301, <http://dx.doi.org/10.1063/1.4824710>.
- [4] B.N. Lucas, W.C. Oliver, Time dependent indentation testing at non-ambient temperatures utilizing the high temperature mechanical properties microprobe, *MRS Proc.* 356 (1995) 645–650, <http://dx.doi.org/10.1557/PROC-356-645>.
- [5] J.F. Smith, S. Zheng, High temperature nanoscale mechanical property measurements, *Surf. Eng.* 16 (2000) 143–146, <http://dx.doi.org/10.1179/026708400101517044>.
- [6] B.D. Beake, J.F. Smith, High-temperature nanoindentation testing of fused silica and other materials, *Philos. Mag. A.* 82 (2002) 2179–2186, <http://dx.doi.org/10.1080/01418610210134387>.
- [7] J. Xia, C.X. Li, H. Dong, Hot-stage nano-characterisations of an iron aluminate, *Mater. Sci. Eng. A.* 354 (2003) 112–120, [http://dx.doi.org/10.1016/S0921-5093\(02\)00902-4](http://dx.doi.org/10.1016/S0921-5093(02)00902-4).
- [8] D.E. Kramer, K.B. Yoder, W.W. Gerberich, Surface constrained plasticity: oxide rupture and the yield point process, *Philos. Mag. A.* 81 (2001) 2033–2058, <http://dx.doi.org/10.1080/01418610108216651>.
- [9] C.A. Schuh, J.K. Mason, A.C. Lund, Quantitative insight into dislocation nucleation from high-temperature nanoindentation experiments, *Nat. Mater.* 4 (2005) 617–621, <http://dx.doi.org/10.1038/nmat1429>.
- [10] M. Rebelo De Figueiredo, M.D. Abad, A.J. Harris, C. Czettel, C. Mitterer, P. Hosemann, Nanoindentation of chemical-vapor deposited Al<sub>2</sub>O<sub>3</sub> hard coatings at elevated temperatures, *Thin Solid Films* 578 (2015) 20–24, <http://dx.doi.org/10.1016/j.tsf.2015.01.069>.
- [11] N.M. Everitt, M.I. Davies, J.F. Smith, High temperature nanoindentation - the importance of isothermal contact, *Philos. Mag.* 91 (2011) 1221–1244, <http://dx.doi.org/10.1080/14786435.2010.496745>.
- [12] A. Sawant, S. Tin, High temperature nanoindentation of a Re-bearing single crystal Ni-base superalloy, *Scr. Mater.* 58 (2008) 275–278, <http://dx.doi.org/10.1016/j.scriptamat.2007.10.013>.
- [13] J.C. Trenkle, C.E. Packard, C.A. Schuh, Hot nanoindentation in inert environments, *Rev. Sci. Instrum.* 81 (2010) 73901, <http://dx.doi.org/10.1063/1.3436633>.
- [14] S. Korte, W.J. Clegg, Micropillar compression of ceramics at elevated temperatures, *Scr. Mater.* 60 (2009) 807–810, <http://dx.doi.org/10.1016/j.scriptamat.2009.01.029>.
- [15] S. Korte, J.S. Barnard, R.J. Stearn, W.J. Clegg, Deformation of silicon - insights from microcompression testing at 25–500 °C, *Int. J. Plast.* 27 (2011) 1853–1866, <http://dx.doi.org/10.1016/j.ijplas.2011.05.009>.
- [16] S. Korte, R.J. Stearn, J.M. Wheeler, W.J. Clegg, High temperature microcompression and nanoindentation in vacuum, *J. Mater. Res.* 27 (2012) 167–176, <http://dx.doi.org/10.1557/jmr.2011.268>.
- [17] D. Kiener, C. Motz, G. Dehm, R. Pippan, Overview on established and novel FIB based miniaturized mechanical testing using in-situ SEM, *Int. J. Mat. Res.* 100 (2009) 1074–1087, <http://dx.doi.org/10.3139/146.110149>.
- [18] M. Legros, D.S. Gianola, C. Motz, Quantitative in situ mechanical testing in electron Microscopes, *MRS Bull.* 35 (2010) 354–360, <http://dx.doi.org/10.1557/mrs2010.567>.
- [19] D.S. Gianola, C. Eberl, Micro- and nanoscale tensile testing of materials, *Jom.* 61 (2009) 24–35, <http://dx.doi.org/10.1007/s11837-009-0037-3>.
- [20] A.J. Harris, B.D. Beake, D.E.J. Armstrong, M.I. Davies, Development of high temperature nanoindentation methodology and its application in the nanoindentation of polycrystalline tungsten in vacuum to 950 °C, *Exp. Mech.* (2016) 1–12, <http://dx.doi.org/10.1007/s11340-016-0209-3>.
- [21] B. Moser, J. Kuebler, H. Meinhard, W. Muster, J. Michler, Observation of instabilities during plastic deformation by in-situ SEM indentation experiments, *Adv. Eng. Mater.* 7 (2005) 388–392, <http://dx.doi.org/10.1002/adem.200500049>.
- [22] B. Moser, K. Wasmer, L. Barbieri, J. Michler, Strength and fracture of Si micropillars: a new scanning electron microscopy-based micro-compression test, *J. Mater. Res.* 22 (2007) 1004–1011, <http://dx.doi.org/10.1557/jmr.2007.0140>.
- [23] J.M. Wheeler, R. Raghavan, J. Michler, In situ SEM indentation of a Zr-based bulk metallic glass at elevated temperatures, *Mater. Sci. Eng. A.* 528 (2011) 8750–8756, <http://dx.doi.org/10.1016/j.msea.2011.08.057>.
- [24] J.M. Wheeler, J. Michler, Elevated temperature, nano-mechanical testing in situ in the scanning electron microscope, *Rev. Sci. Instrum.* 84 (2013) 45103, <http://dx.doi.org/10.1063/1.4795829>.
- [25] V. Maier, A. Leitner, R. Pippan, D. Kiener, Thermally activated deformation behavior of ufg-Au: environmental issues during long-term and high-temperature nanoindentation testing, *JOM.* 67 (2015) 2934–2944, <http://dx.doi.org/10.1007/s11837-015-1638-7>.
- [26] J.M. Wheeler, D.E.J. Armstrong, W. Heinz, R. Schwaiger, High temperature nanoindentation: the state of the art and future challenges, *Curr. Opin. Solid State Mater. Sci.* 19 (2015) 354–366, <http://dx.doi.org/10.1016/j.cossms.2015.02.002>.
- [27] J.M. Wheeler, P. Brodard, J. Michler, Elevated temperature, in situ indentation with calibrated contact temperatures, *Philos. Mag.* 92 (2012) 3128–3141, <http://dx.doi.org/10.1080/14786435.2012.674647>.
- [28] S.-W. Lee, Y. Cheng, I. Ryu, J.R. Greer, Cold-temperature deformation of nano-sized tungsten and niobium as revealed by in-situ nano-mechanical experiments, *Sci. China Technol. Sci.* 57 (2014) 652–662, <http://dx.doi.org/10.1007/s11431-014-5502-8>.
- [29] A.B. Hagen, C. Thaulow, Low temperature in-situ micro-compression testing of iron pillars, *Mater. Sci. Eng. A.* 678 (2016) 355–364, <http://dx.doi.org/10.1016/j.msea.2016.09.110>.
- [30] A.B. Hagen, B.D. Snartland, C. Thaulow, Temperature and orientation effects on the deformation mechanisms of  $\alpha$ -Fe micropillars, *Acta Mater.* 129 (2017) 398–407, <http://dx.doi.org/10.1016/j.actamat.2017.03.006>.
- [31] A. Lupinacci, J. Kacher, A. Eilenberg, A.A. Shapiro, P. Hosemann, A.M. Minor, Cryogenic in situ microcompression testing of Sn, *Acta Mater.* 78 (2014) 56–64, <http://dx.doi.org/10.1016/j.actamat.2014.06.026>.
- [32] K.V. Rajulapati, M.M. Biener, J. Biener, A.M. Hodge, Temperature dependence of the plastic flow behavior of tantalum, *Philos. Mag. Lett.* 90 (2010) 35–42, <http://dx.doi.org/10.1080/09500830903356893>.
- [33] V. Maier, A. Hohenwarter, R. Pippan, D. Kiener, Thermally activated deformation processes in body-centered cubic Cr - how microstructure influences strain-rate sensitivity, *Scr. Mater.* 106 (2015) 42–45, <http://dx.doi.org/10.1016/j.scriptamat.2015.05.001>.
- [34] O. Torrents Abad, J.M. Wheeler, J. Michler, A.S. Schneider, E. Arzt, Temperature-dependent size effects on the strength of Ta and W micropillars, *Acta Mater.* 103 (2016) 483–494, <http://dx.doi.org/10.1016/j.actamat.2015.10.016>.
- [35] J.M. Wheeler, C. Kirchlechner, J.S. Micha, J. Michler, D. Kiener, The effect of size on the strength of FCC metals at elevated temperatures: annealed copper, *Philos. Mag.* (2016) 1–17, <http://dx.doi.org/10.1080/14786435.2016.1224945>.
- [36] J.M. Wheeler, C. Niederberger, C. Tessarek, S. Christiansen, J. Michler, Extraction of plasticity parameters of GaN with high temperature, in situ micro-compression, *Int. J. Plast.* 40 (2013) 140–151, <http://dx.doi.org/10.1016/j.ijplas.2012.08.001>.
- [37] Granta Design Limited, CES Edupack, 2016.
- [38] S. Wurster, C. Motz, M. Jenko, R. Pippan, Micrometer-sized specimen preparation based on ion slicing technique, *Adv. Eng. Mater.* 12 (2010) 61–64, <http://dx.doi.org/10.1002/adem.200900263>.
- [39] S. Wurster, R. Tremel, R. Fritz, M.W. Kapp, E.-M. Langs, M. Alfreider, C. Ruhs, P.J. Imrich, G. Felber, D. Kiener, Novel methods for the site specific preparation of micromechanical structures, *Prakt. Met. Sonderband.* 46 (2014) 27–36, <http://dx.doi.org/10.3139/147.110331>.
- [40] R. Pippan, S. Scheriau, A. Taylor, M. Hafok, A. Hohenwarter, A. Bachmaier, Saturation of fragmentation during severe plastic deformation, *Annu. Rev. Mater. Res.* 40 (2010) 319–343, <http://dx.doi.org/10.1146/annurev-matsci-070909-104445>.
- [41] R.Z. Valiev, R.K. Islamgaliev, I.V. Alexandrov, Bulk nanostructured materials from severe and plastic deformation, *Prog. Mater. Sci.* 45 (2000) 103–189, [http://dx.doi.org/10.1016/S0079-6425\(99\)00007-9](http://dx.doi.org/10.1016/S0079-6425(99)00007-9).
- [42] R. Fritz, D. Lutz, V. Maier-Kiener, D. Kiener, Interplay between sample size and grain size: single crystalline vs. ultrafine-grained chromium micropillars, *Mater. Sci. Eng. A.* 674 (2016) 626–633, <http://dx.doi.org/10.1016/j.msea.2016.08.015>.
- [43] S. Wurster, C. Motz, R. Pippan, Characterization of the fracture toughness of micro-sized tungsten single crystal notched specimens, *Philos. Mag.* 92 (2012) 1803–1825, <http://dx.doi.org/10.1080/14786435.2012.658449>.
- [44] D. Kiener, W. Grosinger, G. Dehm, On the importance of sample compliance in uniaxial microtesting, *Scr. Mater.* 60 (2009) 148–151, <http://dx.doi.org/10.1016/j.scriptamat.2008.09.024>.
- [45] I. Sneddon, The relation between load and penetration in the axisymmetric Boussinesq Problem for a punch of arbitrary profile, *Int. J. Engng Sci.* 3 (1965) 47–57, [http://dx.doi.org/10.1016/0020-7225\(65\)90019-4](http://dx.doi.org/10.1016/0020-7225(65)90019-4).
- [46] ASTM International, ASTM Standard E399-09, West Conshohocken, PA, 2003.
- [47] S. Wurster, C. Motz, R. Pippan, Notched-cantilever and -tensile testing on the micrometer scale - effects of constraints on plasticity and fracture behaviour, in: *Proc. 18th Eur. Conf. Fract.*, Dresden, 2010.

- [48] ASTM International, ASTM Standard E813–89, West Conshohocken, PA, 2003.
- [49] D.I. Bolef, J. De Klerk, Anomalies in the elastic constants and thermal expansion of chromium single crystals, *Phys. Rev.* 129 (1963) 1063–1067, <http://dx.doi.org/10.1103/PhysRev.129.1063>.
- [50] E.O. Hall, The deformation and ageing of mild and steel: III discussion of results, *Proc. Phys. Soc. B* 64 (1951) 747–753, <http://dx.doi.org/10.1088/0370-1301/64/9/303>.
- [51] N.J. Petch, The cleavage strength of polycrystals, *J. Iron Steel Inst.* 174 (1953) 25–28.
- [52] C. Howard, R. Fritz, M. Alfreider, D. Kiener, P. Hosemann, The influence of microstructure on the cyclic deformation and damage of copper and an oxide dispersion strengthened steel studied via in-situ micro-beam bending, *Mater. Sci. Eng. A* 687 (2017) 313–322, <http://dx.doi.org/10.1016/j.msea.2017.01.073>.
- [53] A.V. Sameljuk, A.D. Vasilev, S.A. Firstov, Low temperature deformation and fracture behaviour of [100] and [110] chromium single crystals, *Int. J. Refract. Met. Hard Mater.* 14 (1996) 249–255, [http://dx.doi.org/10.1016/0263-4368\(95\)00046-1](http://dx.doi.org/10.1016/0263-4368(95)00046-1).
- [54] M.D. Uchic, D.M. Dimiduk, J.N. Florando, W.D. Nix, Sample dimensions influence strength and crystal plasticity, *Science* 305 (2004) 986–989, <http://dx.doi.org/10.1126/science.1098993>.
- [55] D. Wu, J. Zhang, J.C. Huang, H. Bei, T.G. Nieh, Grain-boundary strengthening in nanocrystalline chromium and the Hall-Petch coefficient of body-centered cubic metals, *Scr. Mater.* 68 (2013) 118–121, <http://dx.doi.org/10.1016/j.scriptamat.2012.09.025>.
- [56] B. Sestak, A. Seeger, *Gleitung und Verfestigung in kubisch-raumzentrierten Metallen und Legierungen*, *Zeitschrift Für Met.* 69 (1978) 195–202.
- [57] P. Gumbsch, Brittle fracture and the brittle-to-ductile transition of tungsten, *J. Nucl. Mater.* 323 (2003) 304–312, <http://dx.doi.org/10.1016/j.jnucmat.2003.08.009>.
- [58] B. Gludovatz, S. Wurstler, A. Hoffmann, R. Pippin, A study into the crack propagation resistance of pure tungsten, *Eng. Fract. Mech.* 100 (2013) 76–85, <http://dx.doi.org/10.1016/j.engfracmech.2012.07.021>.
- [59] J. Riedle, P. Gumbsch, H.F. Fischmeister, V.G. Glebovsky, V.N. Semenov, Fracture studies of tungsten single crystals, *Mater. Lett.* 20 (1994) 311–317, [http://dx.doi.org/10.1016/0167-577X\(94\)90036-1](http://dx.doi.org/10.1016/0167-577X(94)90036-1).
- [60] C. Bohnert, S.M. Weygand, N.J. Schmitt, R. Schwaiger, O. Kraft, Orientation dependence of the fracture behavior of single-crystal tungsten, *Procedia Mater. Sci.* 3 (2014) 479–484, <http://dx.doi.org/10.1016/j.mspro.2014.06.080>.
- [61] C. Bohnert, N.J. Schmitt, S.M. Weygand, O. Kraft, R. Schwaiger, Fracture toughness characterization of single-crystalline tungsten using notched micro-cantilever specimens, *Int. J. Plast.* 81 (2016) 1–17, <http://dx.doi.org/10.1016/j.ijplas.2016.01.014>.
- [62] J. Skogsrud, C. Thaulow, Effect of crystallographic orientation on nanomechanical modelling of an iron single crystal cracked cantilever beam, *Mater. Sci. Eng. A* 685 (2017) 274–283, <http://dx.doi.org/10.1016/j.msea.2016.12.060>.
- [63] A. Hohenwarter, S. Wurstler, Deformation and fracture characteristics of ultrafine-grained vanadium, *Mater. Sci. Eng. A* 650 (2016) 492–496, <http://dx.doi.org/10.1016/j.msea.2015.10.052>.
- [64] R. Pippin, A. Hohenwarter, The importance of fracture toughness in ultrafine and nanocrystalline bulk materials, *Mater. Res. Lett.* 4 (2016) 127–136, <http://dx.doi.org/10.1080/21663831.2016.1166403>.
- [65] M. Faleschini, H. Kreuzer, D. Kiener, R. Pippin, Fracture toughness investigations of tungsten alloys and SPD tungsten alloys, *J. Nucl. Mater.* 367–370 (2007) 800–805, <http://dx.doi.org/10.1016/j.jnucmat.2007.03.079>.
- [66] R. Wadsack, R. Pippin, B. Schedler, Chromium- a material for fusion technology, *Fusion Eng. Des.* 58–59 (2001) 743–748, [http://dx.doi.org/10.1016/S0920-3796\(01\)00554-3](http://dx.doi.org/10.1016/S0920-3796(01)00554-3).
- [67] R.W. Margevicius, J. Riedle, P. Gumbsch, Fracture toughness of polycrystalline tungsten under mode I and mixed mode I/II loading, *Mater. Sci. Eng. A* 270 (1999) 197–209, [http://dx.doi.org/10.1016/S0921-5093\(99\)00252-X](http://dx.doi.org/10.1016/S0921-5093(99)00252-X).
- [68] D. Rupp, R. Mönig, P.A. Gruber, S.M. Weygand, Fracture toughness and microstructural characterization of polycrystalline rolled tungsten, *Int. J. Refract. Met. Hard Mater.* 28 (2010) 669–673, <http://dx.doi.org/10.1016/j.ijrmhm.2010.05.006>.
- [69] S. Kobayashi, S.M. Ohr, In situ fracture experiments in b.c.c. metals, *Philos. Mag. A* 42 (1980) 763–772, <http://dx.doi.org/10.1080/01418618008239383>.
- [70] V. Maier, C. Schunk, M. Göken, K. Durst, Microstructure-dependent deformation behaviour of bcc-metals - indentation size effect and strain rate sensitivity, *Philos. Mag.* 95 (2015) 1766–1779, <http://dx.doi.org/10.1080/14786435.2014.982741>.
- [71] Y. Harada, M. Ohmori, Ductile-brittle transition behavior of rolled chromium, *J. Mater. Process. Technol.* 153–154 (2004) 93–99, <http://dx.doi.org/10.1016/j.jmatprotec.2004.04.011>.
- [72] R. Wadsack, R. Pippin, B. Schedler, Structural refinement of chromium by severe plastic deformation, *Fusion Eng. Des.* 66–68 (2003) 265–269, [http://dx.doi.org/10.1016/S0920-3796\(03\)00136-4](http://dx.doi.org/10.1016/S0920-3796(03)00136-4).